Letter

ADVANCED IMAGING

Ultrahigh-speed schlieren photography via diffraction-gated real-time mapping

Xianglei Liu,[a,†] Patrick Kilcullen,[a,†] Youmin Wang,[b] Brandon Helfield,[c] and Jinyang Liang[a,*]

[a]Laboratory of Applied Computational Imaging, Centre Énergie Matériaux Télécommunications, Institut National de la Recherche Scientifique, Université du Québec, Québec, Canada

[b]Reality Laboratory, Meta Platforms, Redmond, USA

[c]Department of Physics, Concordia University, Québec, Canada

Abstract. Single-shot ultrahigh-speed mapping photography is essential for analyzing fast dynamic processes across various scientific disciplines. Among available techniques, optical diffraction has recently been implemented as a nanosecond time gate for mapping photography. Despite attractive features in light throughput and cost efficiency, existing systems in this approach can sense only light intensity with limited sequence depth and imaging speed. To overcome these limitations, we develop diffraction-gated real-time ultrahigh-speed mapping schlieren (DRUMS) photography. Using a digital micromirror device as a coded dynamic two-dimensional blazed grating, DRUMS photography can record schlieren images of transient events in real time at an imaging speed of 9.8 million frames per second and a sequence depth of 13 frames. We present the working principle of DRUMS photography in both theoretical derivation and numerical simulation, and we apply DRUMS photography to the single-shot real-time video recording of laser-induced breakdown in water.

Keywords: ultrahigh-speed imaging; framing photography; dynamic diffraction; schlieren imaging; digital micromirror device.

Received Nov. 19, 2024; revised manuscript received Jan. 20, 2025; accepted Jan. 23, 2025; published online Feb. 27, 2025.

[DOI: 10.3788/AI.2025.50001]

1. Introduction

Single-shot high-speed mapping photography is indispensable for observing transient physical, chemical, and biological processes during their occurrence, offering critical insights into the underlying mechanisms governing these events[1–4]. This approach assigns time-gated frames of a dynamic scene to separate spatial positions so that they can be captured by one or more two-dimensional (2D) detectors. It effectively circumvents the limitations of high-speed burst charge-coupled device (CCD) sensors and cameras[5] and computational high-speed imaging techniques such as compressive multi-aperture complementary metal-oxide-semiconductor (CMOS) image sensors and compressed optical-streaking cameras[6–8], which often struggle with challenges related to the low fill factor of image sensors and/or the complexity of sophisticated image reconstruction algorithms.

Single-shot high-speed mapping photography can be classified into the categories of active illumination[9] and passive detection[10]. Although the capabilities of these two approaches can often be highly complementary, both also suffer from high technical requirements. Active illumination-based methods typically require complex system configurations to transfer temporal information to other domains, such as the optical spectrum[11,12], illumination angle[13], spatial position[14,15], and/or spatial frequency[16,17] either at the illumination source or receiving sensor. Consequently, the elimination of specialized illumination is an attractive feature of passive detection-based approaches that use receive-only ultrafast detectors[18]. To this end, the passive implementation of time-gating and image mapping is often achieved through the introduction of multiple sensors and/or active optical elements, with examples including rotating steering mirrors combined with a CCD camera array[19], multiple beam splitters combined with intensified CCD cameras[20], and the use of image-convertor streak tubes[21]. However, the introduction of multiple sensors and/or active elements often leads to passive

*Address all correspondence to Jinyang Liang, jinyang.liang@inrs.ca

†These authors contributed equally to this work.

detection-based methods to face challenges in light throughput and cost efficiency.

Among recent advancements, a noticeable development is diffraction-gated real-time ultrahigh-speed mapping (DRUM) photography[22]. Using the inter-pattern transition of a digital micromirror device (DMD)[23–27], DRUM photography leverages a sweeping optical diffraction envelope as a nanosecond-level time gate to sequentially extract frames at different time points from distinct diffraction orders. The system can capture a transient event in a single exposure at 4.8 million frames per second (Mfps) and a sequence depth of 7 frames.

Even with these attractive features, the technical specifications of DRUM photography have the potential for improvement. Currently, DRUM photography only records diffraction orders distributed along a single horizontal axis, thus limiting its sequence depth and imaging speed. More significantly, only transitions between uniform DMD patterns (i.e., "all-on" or "all-off") have so far been employed for diffraction gating in DRUM photography, a restriction that imposes an intensity-only image contrast while also overlooking the DMD's ability to serve as a programmable spatial filter[28,29].

To overcome these limitations, we develop DRUM schlieren (DRUMS) photography. First, by leveraging information from both on-axis and off-axis diffraction orders, DRUMS photography doubles the sequence depth and imaging speed of DRUM photography. Second, by recognizing the DMD as a dual-purpose device for both nanosecond-level diffraction gating and Fourier plane spatial filtering, DRUMS photography introduces schlieren imaging[30–32] capabilities to the DRUM photography platform for ultrahigh-speed image acquisition. Benefiting from this ultrahigh-speed schlieren imaging ability, we apply DRUMS photography to the real-time observation of laser-induced breakdown in distilled water.

2. Operating Principle of DRUMS Photography

2.1. System

The DRUMS photography system is schematically illustrated in Fig. 1(a). A 473 nm continuous-wave laser (CNI, MSL-FN-473) serves as the illumination source for probing a transient scene. After passing through front optics chosen to suit the desired field of view (FOV), the transmitted light is reflected by a beam splitter (Thorlabs, BP250) to form an image of the transient scene on the intermediate image plane (IIP). The image is processed by a folded $4f$ imaging system, consisting of a stereoscopic objective lens (Olympus, MVPLAPO2XC, 0.5 NA) and a DMD (Ajile Light Industries, AJD-4500). The DMD features an array of 912×1140 micromirrors of horizontal pitch $p = 10.8$ μm and width $w = 7.3$ μm, each capable of rapidly flipping between two static states with tilt angles of $\theta_{\mathrm{b-off}} = -12°$ (off-state) and $\theta_{\mathrm{b-on}} = +12°$ (on-state) relative to the surface normal on the x'-axis in a few microseconds [Fig. 1(b)]. A "knife-edge" binary pattern, acting as a half-plane filter in the spatial frequency domain, is loaded on the DMD. By maintaining the "off"-state micromirrors and flipping the "on"-state micromirrors, the DMD serves as a coded dynamic 2D blazed grating. Among the many DMD-generated diffraction orders, those that are distributed along and in proximity to the horizontal axis are selected to pass through the stereoscopic objective lens, subsequently landing on spatially separated positions on the IIP. Finally, they are imaged by a relay system, consisting of two lenses (Thorlabs, AC508-100-A and AC508-75-A), to a CMOS camera (Optronis, CP70-1HS-M-1900) that is rotated by approximately 34° to accommodate the recording of a maximal number of diffraction orders by the sensor.

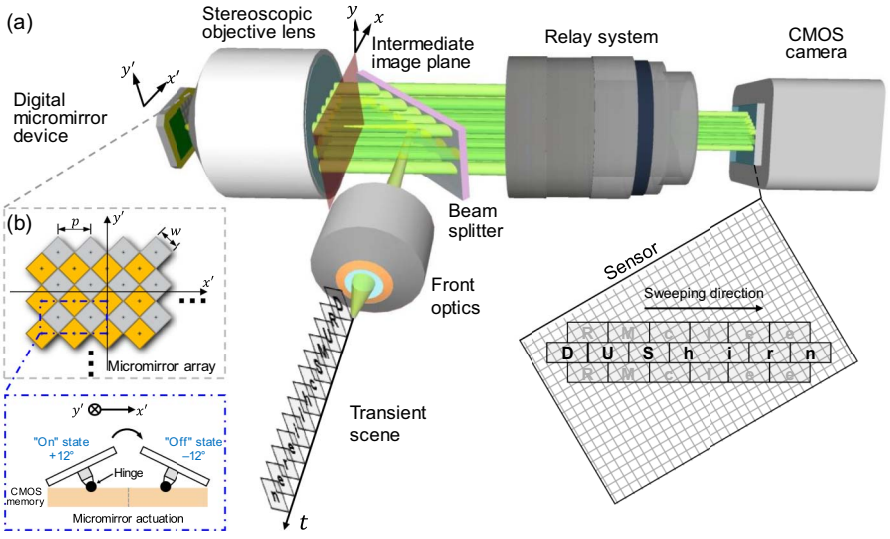

Fig. 1 Schematic of DRUMS photography. (a) Schematic of the system. (b) Schematic of the DMD micromirror array, regarded as the combination of two rectangular grids of pitch p highlighted by the yellow and gray colors. The inset illustrates the flipping action of the DMD micromirrors during pattern transition, with the hinge axis oriented parallel to the y'-axis.

2.2. Derivation of DRUMS image formation

In the following, we assume a unit magnification of the stereoscopic objective lens and the perfect synchronization of the micromirrors' flipping motion. We also ignore aberrations and the finite numerical aperture of the objective lens and relay system. The image of the transient scene created at the IIP by the front optics and beamsplitter is denoted by $O(x, y, t)$. Under the action of the stereoscopic objective lens, the Fourier plane of the IIP is located at the DMD plane. Subsequently, the modulated field at the DMD plane is expressed by

$$U_{\mathrm{DMD}}(x', y', t) = \tilde{O}\left(\frac{x'}{\lambda f}, \frac{y'}{\lambda f}, t\right)[M(x', y', t) \otimes A(x', y')]K(x', y'). \tag{1}$$

Here, λ denotes the wavelength of the continuous-wave laser. f denotes the focal length of the stereoscopic objective lens. "$\otimes$" denotes the 2D convolution. $\tilde{O}(f_x, f_y, t)$ denotes the Fourier transform of the transient scene at the IIP, where the relationships between spatial frequency coordinates and DMD-plane spatial coordinates are expressed as $f_x = \frac{x'}{\lambda f}$ and $f_y = \frac{y'}{\lambda f}$. The three functions $M(\cdot)$, $A(\cdot)$, and $K(\cdot)$ are defined as

$$M(x', y', t) = \mathrm{rect}\left(\frac{x' - y'}{\sqrt{2}w}, \frac{x' + y'}{\sqrt{2}w}\right) \exp\left\{i2\pi x' \frac{\sin[2\theta_{\mathrm{b}}(t)]}{\lambda}\right\}, \tag{2}$$

$$A(x', y') = \mathrm{comb}\left(\frac{x'}{p}, \frac{y'}{p}\right) + \mathrm{comb}\left(\frac{x'}{p} - \frac{1}{2}, \frac{y'}{p} - \frac{1}{2}\right), \tag{3}$$

$$K(x', y') = \mathrm{rect}\left(\frac{x' - x'_k}{L_{\mathrm{KE}}}, \frac{y'}{L'_y}\right). \tag{4}$$

The function $M(\cdot)$ describes the reflection from a square DMD micromirror (of width w) that is both tilted at a time-varying angle of $\theta_{\mathrm{b}}(t)$ relative to normal about the y' axis and oriented at 45° with respect to the x' axis [Fig. 1(b)]. The function $A(\cdot)$ describes the aggregate positioning of the DMD micromirrors as two superimposed rectangular grids of pitch p, where the second grid is shifted by a distance $\frac{p}{2}$ along both the x' and y' axes [Fig. 1(b)]. As a result, the full micromirror array is described by the 2D convolution of $M(\cdot)$ and $A(\cdot)$. Finally, the function $K(\cdot)$ describes the finite rectangular aperture of the DMD, with the width L'_x and the height L'_y restricted for schlieren imaging to a horizontal extent L_{KE} and centered horizontally on the coordinate $x'_k = \frac{L'_x - L_{\mathrm{KE}}}{2}$.

After reflection from the DMD, the stereoscopic lens induces another Fourier transform, mapping the DMD plane to the IIP. Subsequently, the complex field at the IIP is expressed by

$$U_{\mathrm{IIP}}(x, y, t) = O(-x, -y, t) \otimes \left[\tilde{M}\left(\frac{x}{\lambda f}, \frac{y}{\lambda f}, t\right)\tilde{A}\left(\frac{x}{\lambda f}, \frac{y}{\lambda f}\right)\right] \otimes \tilde{K}\left(\frac{x}{\lambda f}, \frac{y}{\lambda f}\right), \tag{5}$$

where the functions $\tilde{M}(\cdot)$, $\tilde{A}(\cdot)$, and $\tilde{K}(\cdot)$ denote the 2D Fourier transforms of $M(\cdot)$, $A(\cdot)$, and $K(\cdot)$, respectively. The appearance of $O(-x, -y, t)$ in Eq. (5) represents the inverted image of the transient scene under unit magnification induced by the folded $4f$ imaging system. The commutativity and associativity of "$\otimes$", together with the properties of the comb$(\cdot)$ function, then allow for the re-expression of Eq. (5), up to proportionality, as

$$\begin{aligned} U_{\mathrm{IIP}}(x, y, t) \propto & \sum_{m=-\infty}^{\infty} \sum_{n=-\infty}^{\infty} \{1 + \cos[\pi(m + n)]\} \\ & \times \mathrm{sinc}\left\{\frac{w}{\sqrt{2}p}\left\{m - n - \frac{p}{\lambda}\sin[2\theta_{\mathrm{b}}(t)]\right\}\right. \\ & \left. \times \frac{w}{\sqrt{2}p}\left\{m + n - \frac{p}{\lambda}\sin[2\theta_{\mathrm{b}}(t)]\right\}\right\} \\ & \times S\left(x - \frac{\lambda f m}{p}, y - \frac{\lambda f n}{p}, t\right), \end{aligned} \tag{6}$$

where the function $S(\cdot)$ is the schlieren image of the transient scene, defined as

$$\begin{aligned} S(x, y, t) = O(-x, -y, t) \otimes \left[\mathrm{sinc}\left(\frac{xL_{\mathrm{KE}}}{\lambda f}, \frac{yL'_y}{\lambda f}\right)\right. \\ \left. \times \exp\left(-i\pi x \frac{2x'_k}{\lambda f}\right)\right]. \end{aligned} \tag{7}$$

Equation (6) thus defines the image produced in the IIP as a 2D array of shifted copies of the schlieren image of the transient scene, each indexed according to integer diffraction order coordinates (m, n) and modulated by an intensity envelope with a time-varying position parameterized by the micromirror tilt angle $\theta_{\mathrm{b}}(t)$. Due to the presence of the term $\{1 + \cos[\pi(m + n)]\}$ in Eq. (6), diffraction orders with $m + n$ odd are suppressed, producing an effective diffraction pattern of a rectangular grid with a 45° orientation.

Taking the squared modulus of Eq. (6) produces the time-dependent intensity signal $I_{\mathrm{IIP}}(x, y, t)$ imaged by DRUMS photography. Under the assumption that the diffraction orders produced by the DMD are well-spaced relative to the FOV presented by the copies of the schlieren images, the intensity signal can be approximated as a sum of intensities of separate diffraction orders:

$$\begin{aligned} I_{\mathrm{IIP}}(x, y, t) \approx & \sum_{\substack{m,n \in \mathbb{Z} \\ \mathrm{mod}(m+n,2)=0}} \left|S\left(x - \frac{\lambda f m}{p}, y - \frac{\lambda f n}{p}, t\right)\right|^2 \\ & \times \mathrm{sinc}^2\left\{\frac{w}{\sqrt{2}p}\left\{m - n - \frac{p}{\lambda}\sin[2\theta_{\mathrm{b}}(t)]\right\}\right. \\ & \left. \times \frac{w}{\sqrt{2}p}\left\{m + n - \frac{p}{\lambda}\sin[2\theta_{\mathrm{b}}(t)]\right\}\right\}. \end{aligned} \tag{8}$$

Equation (8) thus provides the foundation for DRUMS photography's image acquisition, with the rapid time-dependent positioning of the sinc$^2(\cdot)$ intensity envelope serving as the basis for diffraction-gated ultrahigh-speed imaging. Finally, after the relay of the intensity signal to the camera, image acquisition takes place via the time integration of $I_{\mathrm{IIP}}(x, y, t)$.

2.3. Key parameters

The sequence depth of DRUMS photography is governed by the spacing of diffraction orders on the IIP, together with the swept range of the $\mathrm{sinc}^2(\cdot)$ envelope in Eq. (8). Given the limits $\theta_{\mathrm{b-off}} \le \theta_{\mathrm{b}}(t) \le \theta_{\mathrm{b-on}}$ obeyed by the micromirrors, the range of horizontal diffraction orders swept by the peak of the $\mathrm{sinc}^2(\cdot)$ envelope can be seen to obey $\frac{p}{\lambda}\sin 2\theta_{\mathrm{b-off}} \le m \le \frac{p}{\lambda}\sin 2\theta_{\mathrm{b-on}}$. In this work, the range of on-axis diffraction orders is expressed by $n = 0$ and $m = 0, \pm 2, \pm 4, \pm 6$, and ± 8. Similarly, characterized by Eq. (8), the range of swept off-axis diffraction orders is expressed by $n = \pm 1$ and $m = \pm 1, \pm 3, \pm 5, \pm 7$. In practice, however, the six diffraction orders $(\pm 8, 1)$, $(\pm 7, 1)$, and $(\pm 7, -1)$ were found to be too close to the beam reflection directions in the static "off" and "on" states of the micromirrors, thus resulting in a high background. As a result, these diffraction orders were blocked at the IIP. Noting the equivalence of data produced by off-axis diffraction orders $(m, \pm 1)$, we combined the corresponding images to improve the signal level and mitigate the intensity discrepancy between on-axis and off-axis images. Thus, DRUMS photography achieves a sequence depth of 13 frames.

Assuming that the zero overlap occurs between images produced by adjacent diffraction orders, the FOV of DRUMS photography is determined by the magnification ratio of the front optics M_{obj} and the area allotted to the image associated with each diffraction order at the IIP. Further assuming that these images may each cover a disk with a diameter equal to the minimum space between diffraction orders, the input-space FOV diameter may be expressed by

$$D_{\mathrm{FOV}} = \frac{\sqrt{2}\lambda f}{p M_{\mathrm{obj}}}. \tag{9}$$

By substituting the value $f = 45$ mm and $M_{\mathrm{obj}} = 2.2$–4.0 corresponding to our experiments, the FOV diameter of DRUMS photography was calculated to be $D_{\mathrm{FOV}} =$ 0.70–1.26 mm. It should be noted that a variety of choices of FOV shape and size are compatible with DRUMS photography, depending on how identical regions surrounding each diffraction order are allowed to partition the IIP via the choice of field stop in the optical setup. For example, by partitioning the IIP into horizontally oriented rectangular regions centered on each diffraction order [see the inset in Fig. 1(a)] and using $M_{\mathrm{obj}} = 4.0$ front optics, the DRUMS photography system attained an FOV of size 1.0 mm × 0.5 mm (width × height).

Stemming from the diffraction gating mechanism, the frame rate of DRUMS photography is determined by the time interval separating the arrival of the diffraction envelope's peak intensity at adjacent diffraction orders along the x axis of the IIP. Owing to the shape of the $\mathrm{sinc}^2(\cdot)$ envelope, the arrival time t_m seen by a diffraction order (m, n) can be observed from Eq. (8) to satisfy

$$m - \frac{p}{\lambda}\sin[2\theta_{\mathrm{b}}(t_m)] = 0. \tag{10}$$

Making use of the small angle approximation, together with the assumption that the speed of mirror flipping $\frac{d\theta_{\mathrm{b}}}{dt}$ is constant during the interval $[t_{m_{\min}}, t_{m_{\max}}]$ for the range $m = m_{\min}, \ldots, m_{\max}$ of recorded on-axis diffraction orders, the framerate of DRUMS photography may be expressed as

$$r_{\mathrm{DRUMS}} = \frac{m_{\max} - m_{\min}}{t_{m_{\max}} - t_{m_{\min}}} = \frac{2p}{\lambda}\frac{d\theta_{\mathrm{b}}}{dt}. \tag{11}$$

For our characterization of the framerate of DRUMS photography, the values of $t_{m_{\max}}$ and $t_{m_{\min}}$ were measured directly in the time domain using a photodiode that recorded light from the desired diffraction order during mirror flipping. Consequently, the time interval spanning diffraction orders $(-6, 0)$ and $(6, 0)$ was measured at $t_6 - t_{-6} = 1.23$ µs, yielding a framerate of 9.8 Mfps across 13 frames.

3. Simulation of DRUMS Photography

We numerically simulated DRUMS photography using an animation of "Pacman" [Fig. 2(a)] as the ground truth scene. The animation consisted of 13 frames, each with dimensions of 2000 pixel × 4000 pixel, which were employed to simulate a 1.0 mm × 0.5 mm FOV. To mimic the configuration of a DMD, an array of 93 × 93 micromirrors was simulated with each micromirror, modeled as a perfectly reflective 45°-oriented square covering 44 pixel × 44 pixel of area at the Fourier plane. The simulation of micromirror flipping was achieved by specifying a linear phase profile across each mirror. The fill factor of the micromirror array, chosen to mimic that of the DMD used in the DRUMS photography system, was set at 92%[33]. To illustrate the operation of the simulated DMD array, Fig. 2(b) depicts five close-up phase profiles that correspond to the frames in Fig. 2(a).

For schlieren imaging, a knife-edge filter was applied to the 2D Fourier spectrum of each frame in the ground truth. As an example, Fig. 2(c) illustrates the 2D Fourier spectrum of Frame 7, with the blocked portion of the spectrum represented by the green-dash-filled rectangle. Each filtered spectrum, multiplied with the corresponding DMD modulation profile, was inversely Fourier transformed to produce the schlieren image. Five representative DRUMS photography results are depicted in Fig. 2(d), with the full animated sequence shown in Visualization 1.

To illustrate the effect of schlieren imaging, line profiles extracted from simulation results of Frame 1 and Frame 10 [shown by the light blue horizontal lines in Fig. 2(d)] are compared to the corresponding ground truth profiles in Figs. 2(e) and 2(f), respectively. As the line profiles show, the vertical orientation of the knife-edge, together with the blocking of the central DC component of the 2D Fourier spectrum, produces simulated schlieren images that isolate vertically oriented edge features in the ground truth.

4. Evaluation of System Performance

We positioned a negative USAF 1951 resolution target (Thorlabs, R3L1S4N) at the object plane under continuous-wave illumination to assess DRUMS photography's spatial resolution. A representative non-schlieren image of the target recorded by DRUM photography is shown in Fig. 3(a), with the entire 13-frame sequence recorded by DRUMS photography shown in Fig. 3(b). The system can resolve Group 6 Element 2, corresponding to a spatial resolution of 7 µm. To illustrate the effect of knife-edge filtering by the DMD, line profiles [shown by the light blue line in Fig. 3(b)] extracted from images recorded by DRUM photography and DRUMS photography are presented in Fig. 3(c), corresponding to frames extracted by the $(-6, 0)$ diffraction order at time $t = 0$ µs. Similar to

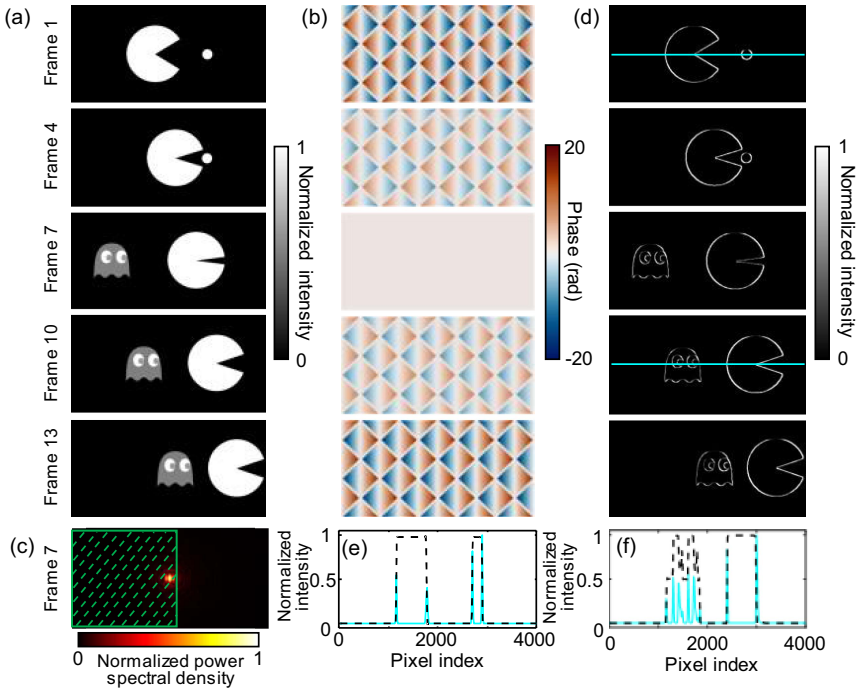

Fig. 2 Simulation of DRUMS photography. (a) Five representative frames of the ground truth dynamic scene. (b) Close-up phase profiles of the simulated DMD during mirror flipping, corresponding to the frames shown in (a). (c) 2D Fourier spectrum of Frame 7 with the portion of spatial frequencies blocked by the knife-edge filter shown by the green-dash-filled rectangle. (d) Simulated frames recorded by DRUMS photography corresponding to the frames and phase profiles shown, respectively, in (a) and (b). (e)–(f) Line profiles [shown by the light blue horizontal lines in (d)] of DRUMS photography (light blue solid line) and the ground truth (black dashed line) in Frame 1 (e) and Frame 10 (f).

the results of the numerical simulation, images recorded by DRUMS photography show the isolation of edge features, demonstrating the system's schlieren imaging capability.

We then conducted proof-of-concept experiments by imaging a fracture defect of a glass microscope slide illuminated by the 473 nm light source modulated with a 2.5 Hz square wave with a 50% duty cycle. A bright-field image recorded by DRUM photography at $t = 0$ μs is shown in Fig. 3(d), with selected frames from the sequence recorded by DRUMS photography shown in Fig. 3(e) and shown fully in Visualization 2. The phase variation caused by the surface discontinuities and rough features, while hardly discernable in the bright-field result, is revealed by DRUMS photography. Finally, the integrated intensity of a selected local region [marked by a light blue rectangle shown in Fig. 3(e)] is provided in Fig. 3(f), showing DRUMS photography's ability to resolve the details of intensity-modulated illumination.

5. Observation of Laser-Induced Breakdown in Liquid

We employed DRUMS photography to investigate the interaction between femtosecond laser pulses and liquid water. In the experimental setup depicted in Fig. 4(a), a single pump pulse (1035 nm wavelength; 350 fs pulse duration; 7 μJ pulse energy) was generated by a femtosecond laser (Huaray, HR-Femto-10) and focused into distilled water contained in a glass cuvette using a lens with a 15 mm focal length (Thorlabs, LB1092). The tightly focused beam ionized the distilled water creating a plasma channel at the focus. Five representative frames recorded by DRUMS photography of the refractive index perturbation caused by the laser-induced breakdown are shown in Fig. 4(b), with the full evolution shown in Visualization 3. The time history of the channel length is illustrated in Fig. 4(c), showing that the channel initiates with a length of 434 μm at 0.23 μs and subsequently decreases to 70 μm at 1.23 μs.

6. Conclusion and Discussion

We have developed DRUMS photography, a single-shot 2D ultrahigh-speed schlieren imaging technique capable of a frame rate of 9.8 Mfps and a sequence depth of 13 frames. By leveraging the abilities afforded by a folded $4f$ imaging system for optical processing together with the inter-pattern transitions of a DMD, this system creates a swept diffraction-based time gate that sequentially extracts frames from 2D diffraction orders. In contrast to traditional DMD-based optical processors[34–38] that operate via sequences of statically displayed patterns at the Fourier plane, the inter-pattern transitions utilized by DRUMS photography realize a form of intrinsically dynamic Fourier plane filtering that enables the simultaneous implementation of ultrahigh-speed imaging with $4f$ optical processing. Meanwhile, leveraging the DMD's programming flexibility, a "knife-edge" filter is implemented to effectively block half of the spatial frequency content along with the DC component to sense the phase gradient of the transient scene. We carried

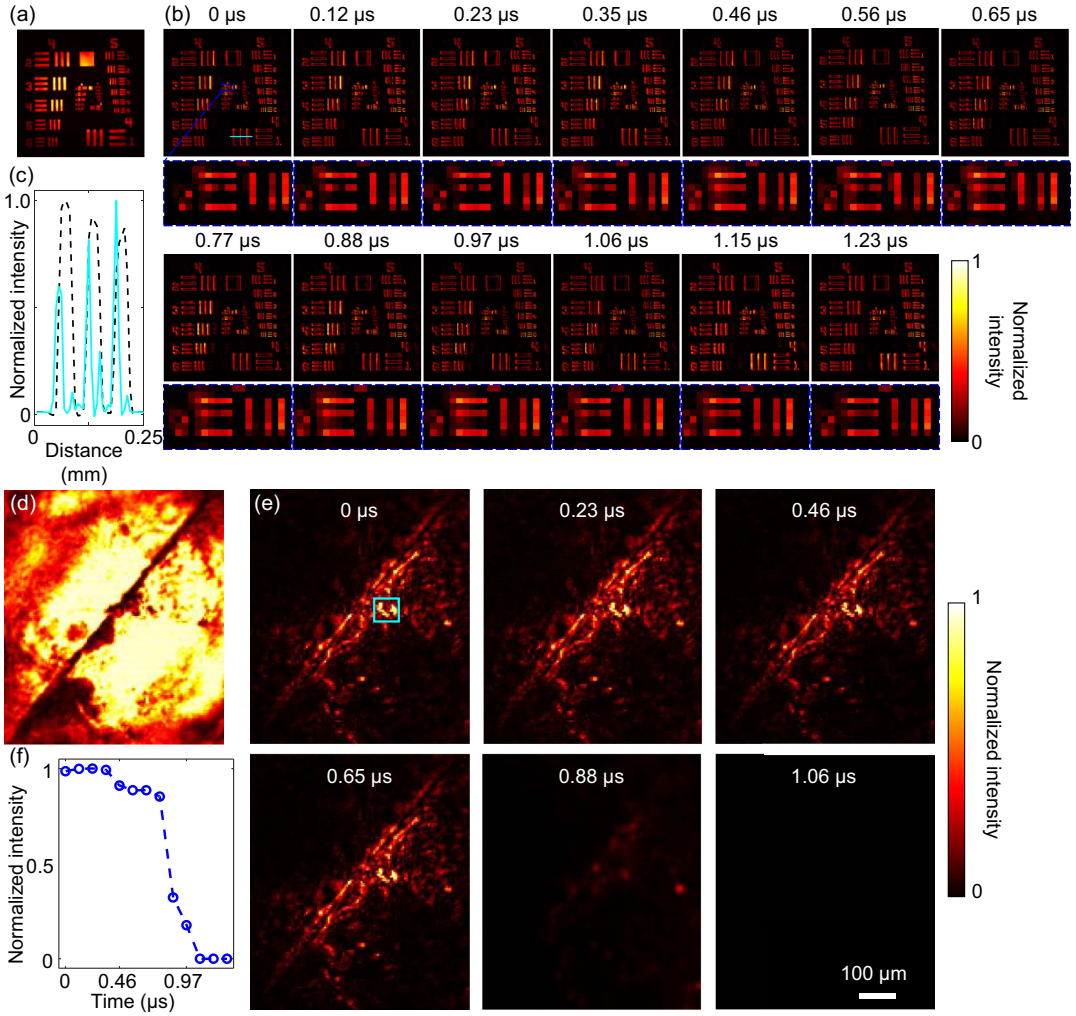

Fig. 3 Characterization of the performance of DRUMS photography. (a) DRUM photography of the USAF 1951 resolution target under continuous-wave illumination. (b) DRUMS photography corresponding to the resolution target in (a). Close-up views show the details of Group 6 Element 2. (c) Comparison of line profiles of Group 4 Element 1 [shown by the light blue line in (b)] between DRUM photography (black dashed line) and DRUMS photography (blue solid light line). (d) DRUM photography of a fracture in a glass microscope slide under continuous-wave illumination modulated with a 50% duty cycle square wave at 2.5 Hz. (e) DRUMS photography corresponding to the scene in (d). (f) Time history of the normalized light intensity of the local region marked by a light blue rectangle in (e).

out theoretical derivation, numerical simulation, and experimental validation of DRUMS photography. The technique was applied to the study of laser-liquid interactions.

DRUMS photography represents one of the fastest schlieren photography systems. Unlike existing setups in this category[39,40], DRUMS photography is developed upon the normal operation of a camera. It retains the advantage of high sensitivity in many scientific-grade cameras (e.g., electron-multiplying CCD cameras and scientific CMOS cameras) and endows them with ultrahigh imaging speeds. In contrast to computational high-speed imaging techniques that employ spatial domain encoding and reconstruction algorithms for the recovery of transient scenes, DRUMS photography avoids the computational overheads associated with compressive reconstruction, as well as the limitations in spatial resolution imposed by the use of spatial domain coded apertures and the inherently ill-posed nature of inverse problems confronted by such techniques in recovering high-dimensionality datasets from low-dimensionality information. Moreover, implemented in a single camera, DRUMS photography embodies a compact and cost-efficient system compared to its counterparts requiring multiple cameras and/or active optical elements[41,42]. Furthermore, the programmable nature of the deployed DMD—as a coded 2D dynamic blazed grating[43]—permits the customization of imaging parameters tailored to specific experimental requirements, further enhancing the system's adaptability. In terms of repeatability and long-term stability, DRUMS photography benefits directly from the well-established reliability and robustness of DMD hardware, with demonstrated operation lifetimes exceeding 100,000 h and 3 trillion display cycles[44]. Benefitting from a

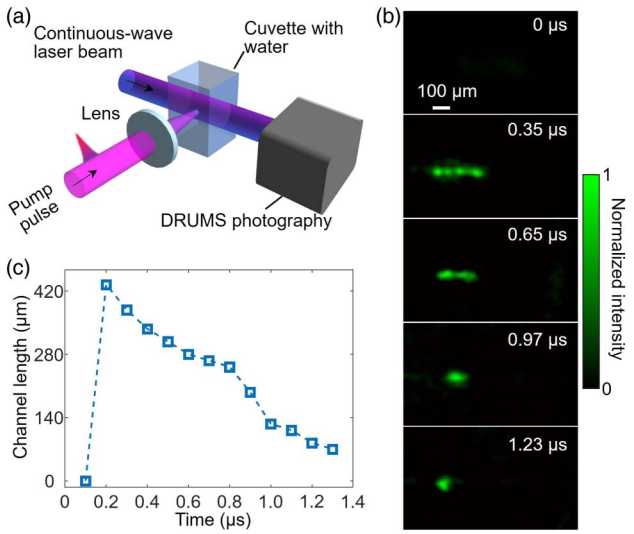

Fig. 4 DRUMS photography of laser-induced breakdown in distilled water. (a) Schematic of the experimental setup. (b) Selected DRUMS photography frames showing the evolution of the laser-induced plasma channel in distilled water using a 7 μJ pump pulse. (c) Time history of the channel length.

non-mechanical knife-edge filter, DRUMS photography features high accuracy and flexibility in system alignment and calibration. Finally, considering the broad responsive spectrum of the DMD, DRUMS photography possesses high adaptability to dynamic scenes at different wavelengths.

Future work will be carried out in the following three aspects. First, we plan to further enhance the system's imaging speed using micro-electro-mechanical system technology with a shorter inter-pattern transition[45]. Second, although demonstrated only for schlieren imaging, DRUMS photography could be applied to phase-sensitive microscopy by loading a rotationally symmetric filter on the DMD[46]. Finally, we plan to apply DRUMS photography to study the impact of tissue heterogeneity on laser ablation for minimally invasive surgeries[47].

Disclosures

The authors declare no competing interests in this work.

Code and Data Availability

All data are available from the corresponding author upon reasonable request.

Authors' Contributions

X. L. built the system and performed the experiments. P. K., X. L., and J. L. developed the theory. X. L. and P. K. analyzed the data and drafted the manuscript. J. L. conceived the concept and designed the system. J. L., B. H., and Y. W. initiated the project. All authors revised the manuscript.

Acknowledgments

This work was supported by the Natural Sciences and Engineering Research Council of Canada (No. RGPIN-2024-05551), the Canada Research Chairs Program (No. CRC-2022-00119), and the Fonds de recherche du Québec–Nature et technologies (No. 203345 - Centre d'optique, photonique et lasers).

References

1. Y. Yao, *et al.*, "Capturing transient events in series: a review of framing photography," *Laser Photonics Rev.* **18**, 2400219 (2024).
2. T. Saiki, *et al.*, "Single-shot optical imaging with spectrum circuit bridging timescales in high-speed photography," *Sci. Adv.* **9**, eadj8608 (2023).
3. M. Sheinman, *et al.*, "Flatfield ultrafast imaging with single-shot non-synchronous array photography," *Opt. Lett.* **47**, 577 (2022).
4. S. Ek, *et al.*, "High-speed videography of transparent media using illumination-based multiplexed schlieren," *Sci. Rep.* **12**, 19018 (2022).
5. L. Lazovsky, *et al.*, "CCD sensor and camera for 100 Mfps burst frame rate image capture," in *Proc. SPIE* **5787**, Airborne Intelligence, Surveillance, Reconnaissance (ISR) Systems and Applications II (2005), pp. 184–190.
6. F. Mochizuki, *et al.*, "Single-event transient imaging with an ultra-high-speed temporally compressive multi-aperture CMOS image sensor," *Opt. Express* **24**, 4155 (2016).
7. X. Liu, *et al.*, "Single-shot real-time compressed ultrahigh-speed imaging enabled by a snapshot-to-video autoencoder," *Photonics Res.* **9**, 2464 (2021).
8. Y. Lai, *et al.*, "Tutorial on compressed ultrafast photography," *J. Biomed. Opt.* **29**, S11524 (2024).
9. X. Zeng, *et al.*, "Review and prospect of single-shot ultrafast optical imaging by active detection," *Ultrafast Sci.* **3**, 0020 (2023).
10. J. Liang and L. V. Wang, "Single-shot ultrafast optical imaging," *Optica* **5**, 1113 (2018).
11. X. Zeng, *et al.*, "High-spatial-resolution ultrafast framing imaging at 15 trillion frames per second by optical parametric amplification," *Adv. Photonics* **2**, 056002 (2020).
12. Y. Yao, *et al.*, "Single-shot real-time ultrafast imaging of femtosecond laser fabrication," *ACS Photonics* **8**, 738 (2021).
13. H.-Y. Huang and C.-S. Guo, "Simple system for realizing single-shot ultrafast sequential imaging based on spatial multiplexing in-line holography," *Opt. Express* **30**, 41613 (2022).
14. S. Yeola, D. Kuk, and K.-Y. Kim, "Single-shot ultrafast imaging via spatiotemporal division of femtosecond laser pulses," *JOSA B* **35**, 2822 (2018).
15. L. Yan, *et al.*, "Multi-frame observation of a single femtosecond laser pulse propagation using an echelon and optical polarigraphy technique," *IEEE Photonics Technol. Lett.* **25**, 1879 (2013).
16. S. Ek, V. Kornienko, and E. Kristensson, "Long sequence single-exposure videography using spatially modulated illumination," *Sci. Rep.* **10**, 18920 (2020).
17. M. Gragston, *et al.*, "Single-shot nanosecond-resolution multi-frame passive imaging by multiplexed structured image capture," *Opt. Express* **26**, 28441 (2018).
18. "Multi-Channel ICCD Framing Camera | XXRapidFrame," https://stanfordcomputeroptics.com/products/iccd-framing-camera.html
19. E. C. Gelderblom, *et al.*, "Brandaris 128 ultra-high-speed imaging facility: 10 years of operation, updates, and enhanced features," *Rev. Sci. Instrum.* **83**, 103706 (2012).
20. Y. Fang, *et al.*, "A four-channel ICCD framing camera with nanosecond temporal resolution and high spatial resolution," *J. Mod. Opt.* **68**, 661 (2021).
21. G. D. Fuchs, *et al.*, "Excited-state spin coherence of a single nitrogen–vacancy centre in diamond," *Nat. Phys.* **6**, 668 (2010).
22. X. Liu, *et al.*, "Diffraction-gated real-time ultrahigh-speed mapping photography," *Optica* **10**, 1223 (2023).
23. B. Smith, *et al.*, "Single chip lidar with discrete beam steering by digital micromirror device," *Opt. Express* **25**, 14732 (2017).

24. B. Hellman, *et al.*, "Single-chip holographic beam steering for lidar by a digital micromirror device with angular and spatial hybrid multiplexing," *Opt. Express* **28**, 21993 (2020).
25. B. Hellman and Y. Takashima, "Angular and spatial light modulation by single digital micromirror device for multi-image output and nearly-doubled étendue," *Opt. Express* **27**, 21477 (2019).
26. D. M. Benton, "Multispectral lidar using a two-dimensional dynamic diffraction grating: how to get nanosecond resolution from a projector and a camera," in *Proc. SPIE* **13200**, Electro-Optical and Infrared Systems: Technology and Applications XXI (2024), pp. 58–67.
27. D. M. Benton, "Temporal and spectral dispersion of an optical source using a micromirror array-based streak camera," *Opt. Eng.* **61**, 114108 (2022).
28. J. Liu, *et al.*, "Coded-aperture broadband light field imaging using digital micromirror devices," *Optica* **8**, 139 (2021).
29. D. Jin, *et al.*, "Dynamic spatial filtering using a digital micromirror device for high-speed optical diffraction tomography," *Opt. Express* **26**, 428 (2018).
30. G. S. Settles and M. J. Hargather, "A review of recent developments in schlieren and shadowgraph techniques," *Meas. Sci. Technol.* **28**, 042001 (2017).
31. G. S. Settles, *Schlieren and Shadowgraph Techniques* (Springer Berlin Heidelberg, 2001).
32. L. M. Weinstein, "Large-field high-brightness focusing schlieren system," *AIAA Journal* **31**, 1250–1255 (1993).
33. Texas Instruments, "DLP4500 .45 WXGA DMD" (datasheet). https://www.ti.com/lit/ds/symlink/dlp4500.pdf?ts=1676164254361
34. T.-H. Chao, H. Zhou, and G. F. Reyes, "Compact 512 × 512 grayscale optical correlator," in *Proc. SPIE* **4734**, Optical Pattern Recognition XIII (2002), pp. 9–12.
35. H. Zhou, *et al.*, "On the development of filter management module for grayscale optical correlator," *Proc. SPIE* **5437**, Optical Pattern Recognition XV (2004), pp. 87–94.
36. T.-H. Chao, *et al.*, "High-speed optical processing using digital micromirror device," *Proc. SPIE* **9094**, Optical Pattern Recognition XXV, 909402 (2014).
37. C. Gu, *et al.*, "Digital micromirror device-based ultrafast pulse shaping for femtosecond laser," *Opt. Lett.* **40**, 2870 (2015).
38. M. Miscuglio, *et al.*, "Massively parallel amplitude-only Fourier neural network," *Optica* **7**, 1812–1819 (2020).
39. H. Kleine, "Filming the invisible–time-resolved visualization of compressible flows," *Eur. Phys. J. Spec. Top.* **182**, 3–34 (2010).
40. H. Kleine, *et al.*, "Time-resolved visualization of shock–vortex systems emitted from an open shock tube," *J. Vis.* **13**, 33–40 (2010).
41. J. Zheng, *et al.*, "A high-performance visible framing ICCD camera base on the image intensifier," in *2023 24th International Conference on Electronic Packaging Technology (ICEPT)* (2023), pp. 1–5.
42. X. Chen, *et al.*, "Ultra-fast bright field and fluorescence imaging of the dynamics of micrometer-sized objects," *Rev. Sci. Instrum.* **84**, 063701 (2013).
43. D. M. Benton, "Multiple beam steering using dynamic zone plates on a micromirror array," *Opt. Eng.* **57**, 073109 (2018).
44. M. Douglass, "DMD reliability: a MEMS success story," in *Proc. SPIE* **4980**, Reliability, Testing, and Characterization of MEMS/MOEMS II (2003).
45. O. Tzang, *et al.*, "Wavefront shaping in complex media with a 350 kHz modulator via a 1D-to-2D transform," *Nat. Photonics* **13**, 788–793 (2019).
46. T. Kim, *et al.*, "Picosecond-resolution phase-sensitive imaging of transparent objects in a single shot," *Sci. Adv.* **6**, eaay6200 (2020).
47. R. Geoghegan, *et al.*, "Methods of monitoring thermal ablation of soft tissue tumors–A comprehensive review," *Med. Phys.* **49**, 769–791 (2022).